Schwank, M., Mätzler, C., Guglielmetti, M., Flühler, H. (2005): L-Band Radiometer Measurements of Soil Water under Growing Clover Grass. - IEEE Transactions on Geoscience and Remote Sensing, 43, 10, 2225-2237

DOI: 10.1109/TGRS.2005.855135

L-Band Radiometer Measurements of Soil Water Under Growing Clover Grass

Mike Schwank, Christian Mätzler, *Senior Member, IEEE*, Massimo Guglielmetti, and Hannes Flühler

***Abstract*—A field experiment with an L-band radiometer at 1.4 GHz was performed from May–July 2004 at an experimental site near Zurich, Switzerland. Before the experiment started, clover grass was seeded. Thermal infrared, *in situ* temperature, and time-domain reflectometer (TDR) measurements were taken simultaneously with hourly radiometer measurements. This setup allowed for investigation of the microwave optical depths and mode opacities (parallel and perpendicular to the soil surface) of the clover grass canopy. Optical depths and opacities were determined by *in situ* analysis and remotely sensed measurements using a nonscattering radiative transfer model. Due to the canopy structure, optical depth and opacity depend on the polarization and radiometer direction, respectively. A linear relation between vegetation water-mass equivalent and polarization-averaged optical depth was observed. Furthermore, measured and modeled radiative transfer properties of the canopy were compared. The model is based on an effective-medium approach considering the vegetation components as ellipsoidal inclusions. The effect of the canopy structure on the opacities was simulated by assuming an anisotropic orientation of the vegetation components. The observed effect of modified canopy structure due to a hail event was successfully reproduced by the model. It is demonstrated that anisotropic vegetation models should be used to represent the emission properties of vegetation. The sensitivity of radiometer measurements to soil water content was investigated in terms of the fractional contribution of radiation emitted from the soil to total radiation. The fraction of soil-emitted radiation was reduced to approximately 0.3 at the most developed vegetation state. The results presented contribute toward a better understanding of the interaction between L-band radiation and vegetation canopies. Such knowledge is important for evaluating data generated from future satellite measurements.**

***Index Terms*—Microwave measurements, microwave radiometry, remote sensing, soil, soil measurements, soil moisture, vegetation.**

I. Introduction

THE large-scale water content distribution is a critical factor for determining the amount of actual evaporation and therefore a driving force in the feedback loop from soil to atmosphere. Because of its importance for questions within the fields of hydrology and climatology, considerable effort has gone into the development of measurement techniques to determine soil water content at larger scales [1]. In [2], the potential of microwave radiometry to measure surface soil moisture was demonstrated. Furthermore, the need for an improved quantitative understanding of the relevant emission and absorption processes explaining measured radiance was identified. This need remains relevant today. In the framework of near-future L-band satellite programs (the Soil Moisture and Ocean-Salinity (SMOS) mission of the European Space Agency [1], [3] and Hydros [4] of the National Aeronautics and Space Administration) it is important to improve knowledge on how microwave radiation interacts with vegetation.

Microwave radiometry at 1.4 GHz [5]–[7] is one of the most promising passive remote sensing techniques to determine soil water content at large scales for the following reasons: 1) absorption by the atmosphere and clouds is almost negligible, allowing for all-weather measurements; 2) vegetation canopies are semitransparent, which enables measurement through vegetation; 3) the measurements are not influenced by solar radiation, which makes it possible to perform day and night observations; and 4) the 1.4-GHz band is protected, avoiding measurement disturbance via human interference.

Microwave radiometry makes use of electromagnetic (EM) energy that is reflected and emitted by the observed scene. At microwave frequencies the measured radiance is proportional to the thermodynamic temperature and emissivity of the surface (Rayleigh–Jeans approximation of Planck's Law). The emissivity is a strong function of the soil water content due to the large contrast between the permittivity of free water (≈ 80), and dry soil (≈ 3 to 5). This allows determination of soil surface-water content from its emissivity by applying dielectric mixing [8] and radiative transfer models. In the simplest case, the soil emissivity is represented by the Fresnel equations [5].

However, more sophisticated models are required for interpretation of radiometer data obtained from observations of complex landscape structures. Several passive remote sensing experiments have been carried out in order to study the microwave emission from natural soils [9]–[11] and the microwave interaction with vegetation [12]–[14].

In [15], early results from microwave radiation measurements of the earth's surface in the presence of vegetation are presented. Thereby, the canopy optical depth was related to some biometric parameters of the vegetation. As demonstrated in [16], soil moisture retrieval by radiometry is possible even if there is a vegetation canopy present, provided that the effects of the vegetation are considered. A simple model was used to account for particular vegetation by relating the vegetation optical depth to the specific water mass equivalent stored in the vegetation.

Manuscript received February 25, 2005; revised June 2, 2005. This work was supported by the Institute of Technology (ETH) Zurich.

M. Schwank, M. Guglielmetti, and H. Flühler are with the Institute of Terrestrial Ecology, Federal Institute of Technology (ETH) Zürich, 8092 Zürich, Switzerland (e-mail: mike.schwank@env.ethz.ch; massimo.guglielmetti@env.ethz.ch; fluehler@env.ethz.ch).

C. Mätzler is with the Institute of Applied Physics, University of Bern, 3012 Bern, Switzerland (e-mail: christian.matzler@mw.iap.unibe.ch).

Digital Object Identifier 10.1109/TGRS.2005.855135

Hornbuckle *et al.* [17] investigated the anisotropy in 1.4-GHz brightness emitted by a corn field. They found that measurements at both polarizations are isotropic in azimuth during most of the growing season. When the canopy is senescent, the L-band measurements were a strong function of vegetation structure. Furthermore, the 1.4-GHz brightness was observed to depend on the radiometer elevation, which was interpreted to be a consequence of volume scattering within the canopy. However, it was found that neglecting scattering is appropriate, because fitted scattering coefficients in the model applied in [17] were small.

A discrete model for the interaction of forest canopies with L-band radiation is described in [18] and [19]. This model considers structural features like branch-, trunk-, and leaf-geometry by means of dielectric oblate spheroids and cylinders.

In this work, we present simultaneously measured ground-truth and remotely sensed measurements evaluated by applying a nonscattering radiative transfer model. Canopy opacities derived from measurements are compared with model calculations based on an anisotropic effective medium model characterizing the canopy at different states. The motivation of this work was to gain insights into the interaction between microwave radiation and vegetation canopies. This is important for soil moisture retrieval on vegetated territories using L-band radiometry. Results of this investigation show that anisotropic mixing models are required for representing dielectric and emission properties of vegetation, indicating that anisotropy and polarization effects are key features of vegetation.

II. Field Experiment

The experiment was carried out on a field site at the Institute of Plant Sciences, Eschikon (550 m a.s.l.), 15 km northeast of Zurich. The measurements were taken between May 27, 2004 (= day of year 148) and July 27, 2004 (= day of year 209). The entire dataset measured during this campaign can be requested from the corresponding author (mike.schwank@env.ethz.ch). Fig. 1 shows the L-band (1.4 GHz) microwave radiometer ELBARA [20] mounted on the tower and the approximate location from which ground-truth measurements were taken during the 61 days of the experiment.

The remote sensing system, the equipment used for the ground-truth measurements, and the conditions at the field site are described below.

A. Remote Sensing System

The microwave radiometer ELBARA operating at 1.4 GHz was designed for remote sensing at the field scale. ELBARA is a Dicke-type radiometer with internal hot and cold loads stabilized at 338 and 278 K for calibration purposes before any measurement. The radiometer is equipped with a dual-polarized conical horn antenna with -3-dB full-beamwidth of 12° and symmetrical and identical beams with small sidelobes. To detect man-made EM noise, ELBARA works simultaneously at two overlapping channels, one between 1400–1418 MHz and the other between 1409–1427 MHz. A more detailed description of the radiometer is reported in [20].

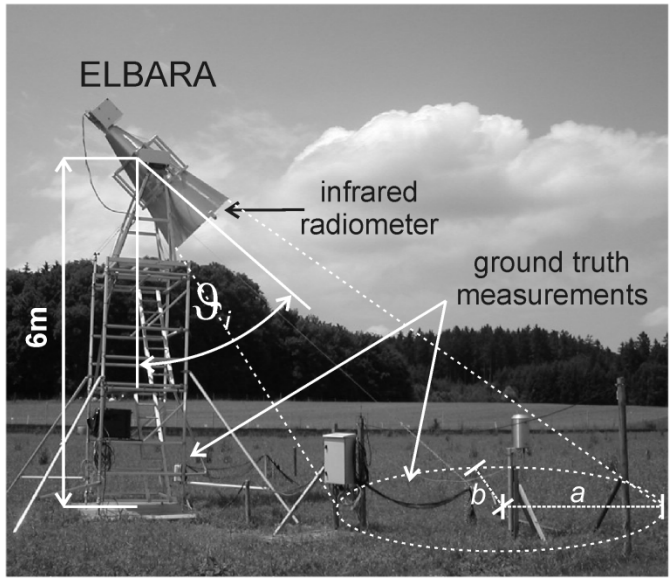

Fig. 1. L-band radiometer ELBARA mounted on the tower at the test site. The half-axes a and b of the elliptic footprint for the incidence angles ϑ_i are given in Table I.

TABLE I
Footprint Dimensions at Incidence Angles ϑ_i. The Measurements Performed at the Highlighted Angles ϑ_1 to ϑ_4 Are Evaluated

ϑ_i [°]	a [m]	b [m]	$d_{\min}$ [m]	$d_{\max}$ [m]	A [m^2]
45	1.27	0.90	4.86	7.41	3.61
50	1.55	1.00	5.79	8.90	4.86
55	1.96	1.12	6.90	10.8	6.93
60	2.61	1.30	8.26	13.5	10.7
65	3.72	1.57	10.0	17.4	18.4
70	5.88	2.01	12.3	24.1	37.2
75	11.1	2.88	15.6	37.9	100.7

The radiometer is attached to an elevation scanning stage mounted on a tower. Incidence angles ϑ between 45° and 140° can be realized, and the center of rotation is 6 m above ground (Fig. 1). This setup allows for automated radiometric observations with variable incidence angles ϑ_i between 45° and 140°. We performed measurements at angles between 45° and 75° with an increment of 5° and sky measurements at 140°. The half axes a and b of the elliptic footprint (Fig. 1) were estimated corresponding to the -3-dB beamwidth, the installation height, and the incidence angle ϑ_i. Furthermore, the horizontal distances $d_{\min}$ and $d_{\max}$, measured from the radiometer to the closest and the farthest footprint border and the footprint areas A, are listed in Table I. However, the data analysis is restricted to the angles $\vartheta_1 = 45°$, $\vartheta_2 = 50°$, $\vartheta_3 = 55°$, and $\vartheta_4 = 60°$ due to increasing reflected sky radiance at angles larger than 60°.

The reliability of the remote sensing system was tested once a day by measuring the zenith radiation temperatures $T^p{}_{\text{zenith}}$ at the maximum angle of 140° at midnight and at horizontal ($p = \text{h}$) and vertical ($p = \text{v}$) polarization. Throughout the entire experiment $T^{\text{h}}{}_{\text{zenith}} = 22$ K and $T^{\text{v}}{}_{\text{zenith}} = 29$ K at h- and v-polarization were measured with standard deviations less than 2 K indicating stable operation of the system. However, the

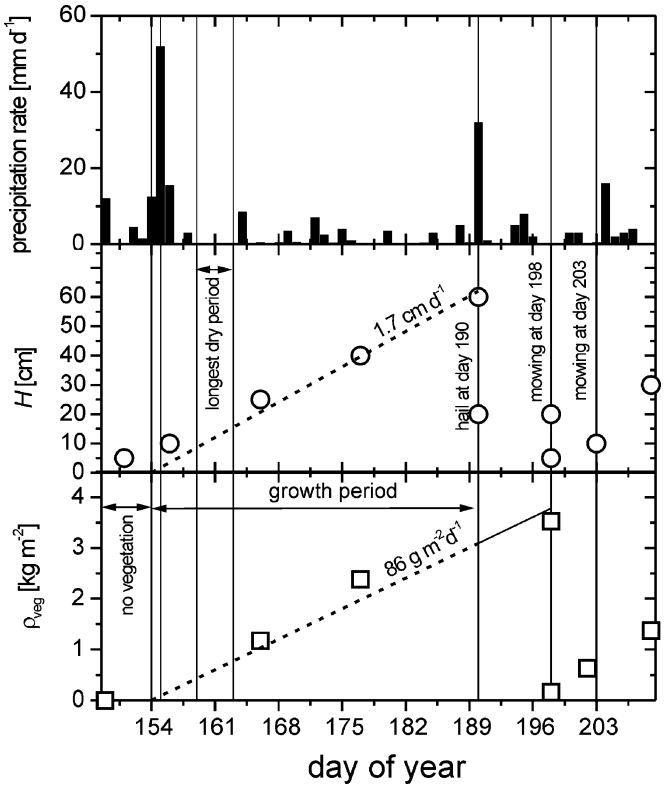

Fig. 2. Precipitation rate [mm $\cdot$ d^{-1}], vegetation height H [cm], and fresh vegetation column density $\rho_{\rm veg}$ [kg $\cdot$ m^{-2}] during the experimental period, May 27, 2004 (= day 148) to July 27, 2004 (= day 209).

polarization-averaged zenith radiation temperature should yield approximately 10 K, which is the sky radiation contribution at L-band. We attribute the difference to device internal absorption occurring in the cable between the antenna and the radiometer receiver. This systematic error and the true sky contribution to the total measured radiation were corrected by referencing all the temperatures to the measured zenith temperatures $T^p{}_{\rm zenith}$ ($p = {\rm h, v}$).

In addition to the L-band measurements, thermal infrared (IR) measurements with the same time resolution were performed. For this purpose, the thermal IR radiometer Everest Interscience 4000.4ZH was attached to the ELBARA antenna (Fig. 1). This IR radiometer is sensitive in the spectral range from 8–15 μm, the temperature range is 243–1033 K, and the accuracy is $\pm 1.0\%$ of reading. The aperture angle is $\pm 7.5°$, which is of the same order as ELBARA's field of view ($\pm 6°$).

B. Ground-Truth Measurements

Hourly ground-truth measurements at two locations close to the radiometer tower were performed. Soil permittivities (related to soil water content) and temperatures were measured *in situ* with horizontally installed two-rod TDR probes (in-house constructed probes (rod length 18 cm, rod diameter 0.2 cm, rod separation 2.5 cm) connected to Campbell TDR100 reflectometer and CR10X datalogger) and thermistors (Campbell S-TL107). At both locations (Fig. 1), these sensors were placed horizontally at seven local depths (2, 4, 6, 10, 20, 30, and 50 cm).

Fig. 3. Clover grass vegetation before and after the hail event on day 190.

C. Field Site Conditions

The experiment was carried out on a flat agricultural area at the Institute of Plant Sciences, Eschikon (550 m a.s.l.), 15 km northeast of Zurich. From the outset of the experiment on May 27, 2004 (day 148) to July 27, 2004 (day 209), the mean temperature measured directly above the soil surface was 18.1 °C.

Total precipitation during the experiment was 224.8 mm. Precipitation rate, vegetation height H, and fresh vegetation mass column density $\rho_{\rm veg}$ measured during the experiment are shown in Fig. 2. The most distinct precipitation events occurred on days 155 and 190 with 55 mm $\cdot$ d^{-1} and 32 mm $\cdot$ d^{-1}, respectively, where the latter was a hailstorm. The longest period without precipitation lasted from day 159 to 163.

At commencement of the experiment, 3.6 g$\cdot$m^{-2} of the clover grass mixture UFA 106 was seeded (= 2 g$\cdot$m^{-2} Lolium westerwoldicum, 1 g$\cdot$m^{-2} *Trifolium alexandrinum*, and 0.6 g$\cdot$m^{-2} *Trifolium resupinatum*). Before seeding, the bare soil was rolled allowing the soil surface to be considered electromagnetically flat. During the first seven days of the experiment (before day 154) the soil was bare. An increasing soil roughness in the course of the experiment, which might be caused by growing vegetation and drying/wettening cycles, is not considered in our investigation. The vegetation grew with a rate of approximately 1.7 cm $\cdot$ d^{-1} and the fresh column density $\rho_{\rm veg}$ increased with approximately 86 g $\cdot$ m^{-2} $\cdot$ d^{-1}. The dry-matter fraction $m_{\rm d}$, defined as the ratio between the vegetation dry and wet mass, was approximately $m_{\rm d} = 0.15$ kg $\cdot$ kg^{-1} throughout the entire growth period from day 154 to 190. For the first half of the growth period, $\rho_{\rm veg}$ was dominated by clover. At later vegetation states, the shares of clover and blades of grass were similar. Due to hailstorm damage on day 190, the upright height of the canopy was reduced from approximately 60 to 20 cm. Fig. 3 shows the intact and the smashed vegetation before and after the hail event. A few days after the hail, clover sprouts emerged in-between the buckled vegetation. On day 198, the main part

of the vegetation was mowed and harvested leaving the canopy height of approximately 5 cm. Thereby, most of the buckled vegetation was removed. A small area close to the tower was mowed five days later (day 203) to approximately 10 cm corresponding to the height of the rest of the field at this time. This area covered approximately half of the footprint at the steepest angle $\vartheta_1 = 45°$. However, the area mowed later did not reach the same state as the previously mowed area of the field until the end of the experiment.

The soil was classified as a loam according to the U.S. Department of Agriculture classification scheme, consisting of rather compacted subsoil covered by an organic-rich top soil layer of approximately 20 cm. The hydraulic properties of the uppermost 60 cm are summarized in [11].

III. Models

The radiative transfer model presented in Section III-A is used for calculating the vegetation optical depths and opacities from the measurements (Sections IV-B and C) and for estimating the fractional contribution of the radiation emitted from the soil to the measured brightness temperature (Section IV-D). A dielectric mixing approach comprising simple but reasonable parameters is presented for modeling the canopy opacities, also considering the anisotropy of the vegetation structure (Section III-C). These calculations are compared with measurement based data showing the influence of the vegetation structure on the emission properties and vice versa the possible characterization of the vegetation architecture using L-band measurements.

A. Microwave Radiative Transfer Model

Microwave remote sensing makes use of EM energy that is reflected and emitted by the earth's surface [6]. The radiometrically detected signal results from the temperatures and emissivities of the partial spaces contributing to the total radiance entering the aperture of the radiometer antenna. Here, the attenuation of the individual radiances along their paths to the antenna has to be considered. Finally, the received radiance is calculated as the sum of the radiation contributions emitted from the relevant locations.

At microwave frequencies, the Rayleigh–Jeans law applies, implying that the radiance of an emitter is proportional to the temperature. This makes it convenient to use brightness temperature instead of radiance.

In the following, the polarization states are labeled by the superscript indexes $p = \mathrm{h}$ for "horizontal" and $p = \mathrm{v}$ for "vertical" polarization. These notations are common, but somewhat misleading. An electric field vector $\boldsymbol{E}^{\mathrm{v}}$ at v-polarization is defined to be parallel to the plane of incidence. As can be seen in Fig. 5, this means that the field vector $\boldsymbol{E}^{\mathrm{v}}$ referred to as "vertical" polarized comprises both a horizontal and a vertical component $\boldsymbol{E}^{\mathrm{v}} = (E^{\mathrm{vx}}, E^{\mathrm{vz}})$, which might be confusing. A horizontally polarized electric field vector $\boldsymbol{E}^{\mathrm{h}}$ is defined to be perpendicular to the plane of incidence. Consequently, this incongruity in terms of denomination does not appear at h-polarization because the field $\boldsymbol{E}^{\mathrm{h}} = (E^{\mathrm{hx}}, 0)$ is horizontally oriented for all incidence angles ϑ.

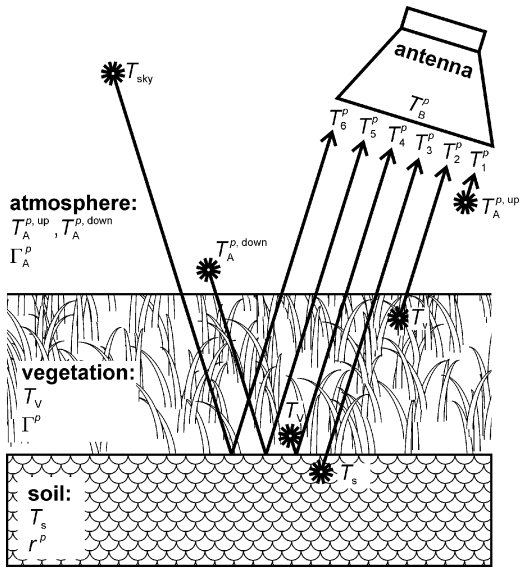

Fig. 4. Sketch of the radiation contributions considered in the radiative transfer model for calculating the brightness temperature $T^p{}_{\mathrm{B}}$ at polarization $p = \mathrm{h}, \mathrm{v}$.

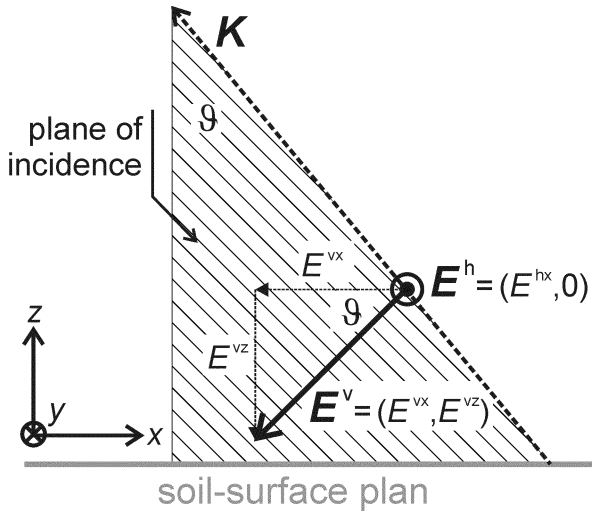

Fig. 5. Sketch of the direction of the electric fields $\boldsymbol{E}^p$ at polarization $p = \mathrm{h}, \mathrm{v}$. $\boldsymbol{K}$ is the propagation vector.

Fig. 4 shows the concept of the microwave radiative model used in this work [21]. Attenuation and emission of the vegetation at polarization $p = \mathrm{h}, \mathrm{v}$ are considered by the transmissivity Γ^p along the line of sight, and scattering-related attenuation is not considered in our investigation [17], [22].

The brightness temperature $T^p{}_{\mathrm{B}}$ at polarization $p = \mathrm{h}, \mathrm{v}$ is given by

$$
\begin{aligned}
&T_{\mathrm{B}}^p = \sum_{i=1}^{6} T_i^p \quad \text{with} \\
&T_1^p = T_{\mathrm{A}}^{p,\mathrm{up}} && T_2^p = T_{\mathrm{v}}\left(1-\Gamma^p\right)\Gamma_{\mathrm{A}}^p \\
&T_3^p = T_{\mathrm{s}}\left(1-r^p\right)\Gamma^p\Gamma_{\mathrm{A}}^p && T_4^p = T_{\mathrm{v}}\left(1-\Gamma^p\right)r^p\Gamma^p\Gamma_{\mathrm{A}}^p \\
&T_5^p = T_{\mathrm{A}}^{p,\mathrm{down}}\left(\Gamma^p\right)^2\Gamma_{\mathrm{A}}^p r^p && T_6^p = T_{\mathrm{sky}}\left(\Gamma^p\Gamma_{\mathrm{A}}^p\right)^2 r^p
\end{aligned} \tag{1}
$$

where $T^p{}_1$ = upward atmospheric emission; $T^p{}_2$ = upward vegetation emission attenuated through atmosphere; $T^p{}_3$ = soil surface emission attenuated through the vegetation and atmosphere; $T^p{}_4$ = downward vegetation emission reflected at

the soil surface and attenuated through the vegetation and atmosphere; $T^p{}_5$ = downward atmospheric emission attenuated through vegetation and atmosphere and reflected at the soil surface; $T^p{}_6$ = sky emission attenuated through vegetation and atmosphere and reflected at the soil surface with reflectivity r^p.

The atmosphere is almost transparent at L-band, and the radiation contribution of the sky is minor [23]. Therefore, the contributions $T^p{}_1$, $T^p{}_5$, and $T^p{}_6$ to the received brightness temperature $T^p{}_\mathrm{B}$ are not considered here.

The expected $T^p{}_\mathrm{B}$ for a bare soil observation is determined by the single term $T^p{}_3$ with atmospheric transmissivity $\Gamma^p{}_\mathrm{A} = 1$

$$T^p_\mathrm{B} = T_\mathrm{s}\,(1 - r^p) \qquad (p = \mathrm{h}, \mathrm{v}). \tag{2}$$

Soil reflectivity r^p is calculated from the dielectric depth profile derived from the *in situ* TDR measurements. A coherent radiative transfer model representing the soil as a stratified dielectric medium of layers with uniform thickness of 1 mm [10], [11] was applied. The calculation is based on a matrix formulation of the boundary conditions at the layer boundaries derived from Maxwell's equations [24].

For accurate calculation of soil temperature T_s relevant for radiation, the temperature profile should be integrated over the temperature sensing depth (20–40 cm at 1 GHz) and weighted according to the total attenuation from any depth to the soil surface [25]. This calculation would require knowledge of the imaginary part of the soil dielectric constant which was not available from the TDR measurements. For this reason, we use the following approximation as proposed in [26]:

$$T_\mathrm{s} = T_{45\ \mathrm{cm}} + (T_{2\ \mathrm{cm}} - T_{45\ \mathrm{cm}}) \cdot C. \tag{3}$$

$T_{2\ \mathrm{cm}}$ and $T_{45\ \mathrm{cm}}$ are the soil temperatures *in situ* measured at 2- and 45-cm depth, respectively, and C is an empirical parameter. We used the best fit value $C = 0.246$ as calculated in [26] based on a large data base for the wavelength of 21 cm. The parameterized equation (3) gives results that are generally within 1% or 2% of the exact value.

The expected L-band brightness temperature $T^p{}_\mathrm{B}$ of a soil covered with vegetation of uniform temperature T_v is the sum of the contributions $T^p{}_2$, $T^p{}_3$, and $T^p{}_4$ given by (1)

$$T^p_\mathrm{B} = T_\mathrm{v}(1-\Gamma^p) + T_\mathrm{s}(1-r^p)\Gamma^p + T_\mathrm{v}(1-\Gamma^p)\,r^p\Gamma^p \ (p = \mathrm{h}, \mathrm{v}). \tag{4}$$

The power transmissivity Γ^p of the vegetation along the line of sight is the positive solution of the above quadratic equation for Γ^p

$$\Gamma^p = -\frac{(T_\mathrm{v}-T_\mathrm{s})(1-r^p) - \sqrt{4r^p(T_\mathrm{v}-T^p_\mathrm{B})T_\mathrm{v} + (T_\mathrm{v}-T_\mathrm{s})^2(1-r^p)^2}}{2r^pT_\mathrm{v}}. \tag{5}$$

Vegetation optical depth τ^p along the line of sight is related to the corresponding Γ^p by Beer's law

$$\Gamma^p = \exp\left(-\tau^p\right) \qquad (p = \mathrm{h}, \mathrm{v}). \tag{6}$$

The above relations will be used for calculating zenith optical depths $\tau^p{}_0 = \tau^p \cos\vartheta_i$ at both polarizations $p = \mathrm{h}, \mathrm{v}$ based on the measurements at incidence angle ϑ_i.

B. Canopy Mode Opacities

Brightness temperatures $T^p{}_\mathrm{B}$ measured at polarization $p = \mathrm{h}, \mathrm{v}$ are proportional to the squared absolute value of the corresponding EM field $\boldsymbol{E}^p$ [6, p. 74]. As mentioned above and illustrated in Fig. 5, the vertically polarized field $\boldsymbol{E}^\mathrm{v} = (E^\mathrm{vx}, E^\mathrm{vz})$ comprises both a component E^vx parallel and a component E^vz perpendicular to the soil-surface plane, if the measurement is performed at any incidence angle $\vartheta \neq 0$.

This instance requires introducing two separate modes given by the projection of the h- and v-polarized fields $\boldsymbol{E}^p$ onto the x–y plane (soil-surface plane) and onto the vertical z direction. The former is denoted as "x mode" and the latter as "z mode." This concept is used for the canopy opacities τ^m effective for the modes $m = \mathrm{x}$ and z (Section IV-C).

Due to the anisotropy of the canopy the effective permittivities ε^m determining the propagation of the x and z mode are different. As a consequence, the canopy opacities τ^m $(m = \mathrm{x}, \mathrm{z})$ for the two modes are different and not equal to the vegetation optical depths derived from the measurements.

For calculating the mode opacities τ^m $(m = \mathrm{x}, \mathrm{z})$ from the measured transmissivities Γ^p $(p = \mathrm{h}, \mathrm{v})$, one has to consider the alignment of the electric fields $\boldsymbol{E}^p$ $(p = \mathrm{h}, \mathrm{v})$ relative to the x–y plane and the z direction.

As can be seen from Fig. 5, the components of the vertically polarized field vector $\boldsymbol{E}^\mathrm{v} = (E^\mathrm{vx}, E^\mathrm{vz})$ are $E^\mathrm{vx} = E^\mathrm{v} \cdot \cos\vartheta_i$ and $E^\mathrm{vz} = E^\mathrm{v} \cdot \sin\vartheta_i$. The field transmission of the x and z mode is affected by the corresponding field transmission coefficient t^m $(m = \mathrm{x}, \mathrm{z})$ of the canopy traversed at the angle ϑ_i.

The transmissivity Γ^v, measured at vertical polarization, is the ratio between powers before and after attenuation which are proportional to $|\boldsymbol{E}^\mathrm{v}|^2$. This allows expression of Γ^v as the squares of the field transmissions t^x and t^z

$$\Gamma^\mathrm{v} = \left(t^\mathrm{x}\cos\vartheta_i\right)^2 + \left(t^\mathrm{z}\sin\vartheta_i\right)^2. \tag{7}$$

The horizontally polarized field $\boldsymbol{E}^\mathrm{h} = (E^\mathrm{hx}, 0)$ comprises the x mode E^hx only. Therefore, the corresponding transmissivity Γ^h is

$$\Gamma^\mathrm{h} = \left(t^\mathrm{x}\right)^2. \tag{8}$$

The field transmission coefficients t^m are expressed using Beer's law

$$t^m = \exp\left(-\frac{\tau^m}{2\cos\vartheta_i}\right) \qquad (m = \mathrm{x}, \mathrm{z}). \tag{9}$$

The factor 2 in the denominator of the exponential is due to the definition of the mode opacities τ^m $(m = \mathrm{x}, \mathrm{z})$ related to the transmissivity instead of the field transmission coefficient [27].

Experimentally based mode opacities τ^m are calculated from the transmissivities Γ^p $(p = \mathrm{h}, \mathrm{v})$ of the canopy deduced from the measurements at h- and v-polarization using the radiative transfer model (5). The canopy opacity affecting the x mode (parallel to the soil-surface plane) is evaluated by combining (8) with (9) and solving for τ^x

$$\tau^\mathrm{x} = -\cos\vartheta_i \log\Gamma^\mathrm{h}. \tag{10}$$

From this, the opacity for the vertical mode τ^{z} is calculated by combining (7) with (9)

$$\tau^{\mathrm{z}} = -\cos\vartheta_i \log \frac{\Gamma^{\mathrm{v}} - \cos^2\vartheta_i \exp\left(-\frac{\tau^{\mathrm{x}}}{\cos\vartheta_i}\right)}{\sin^2\vartheta_i}. \tag{11}$$

The above relations (10) and (11) together with the radiative transfer model (5) will be used in Section IV-C for calculating time-series of mode opacities τ^m ($m = \mathrm{x}, \mathrm{z}$). These measurement-based opacities will be compared with calculated opacities derived from the dielectric mixing approach, characterizing the vegetation canopy presented in Section III-C.

C. Canopy Model

A dielectric mixing approach is applied for estimating the effective dielectric properties ε^m ($m = \mathrm{x}, \mathrm{z}$) of the canopy. According to the anisotropic vegetation structure the permittivity ε^{x} affecting the x mode (parallel to the soil-surface plane) is different from the permittivity ε^{z} relevant for the z mode. From these effective canopy permittivities ε^m ($m = \mathrm{x}, \mathrm{z}$) the corresponding field attenuation coefficients γ^m [m^{-1}] and hence the canopy mode opacities τ^m are calculated.

The general idea of the mixing approach is to represent the vegetation components by dipole moments, which are averaged to obtain the electric polarizability α. The Clausius–Mosotti formula [28] relates the effective permittivity $\varepsilon_{\mathrm{eff}}$ to the polarizability α, the depolarization factor N and the number density n [m^{-3}] of the scatterers embedded in the dielectric background host with dielectric constant ε_{e}

$$\varepsilon_{\mathrm{eff}} = \varepsilon_{\mathrm{e}} + \frac{n\alpha}{1 - \frac{nN\alpha}{\varepsilon_{\mathrm{e}}}}. \tag{12}$$

For mixtures that are highly depleted in the dielectric sense, $nN\alpha/\varepsilon_{\mathrm{e}} \ll 1$ holds. Due to the low volume fraction of the water phase within the considered canopy ($< 1\%$), the above relation can be simplified to

$$\varepsilon_{\mathrm{eff}} \cong \varepsilon_{\mathrm{e}} + n\alpha. \tag{13}$$

For spherical scatterers with volume $V = (4\pi r^3)/3$ (r = radius) and permittivity ε_{i} the polarizability α and the depolarization factor N are given by

$$\alpha = V(\varepsilon_{\mathrm{i}} - \varepsilon_{\mathrm{e}}) \frac{3\varepsilon_{\mathrm{e}}}{\varepsilon_{\mathrm{i}} + 2\varepsilon_{\mathrm{e}}} \quad N = \frac{1}{3}. \tag{14}$$

Substituting this into (12) together with the dimensionless volume fraction $f = nV$ of the inclusions in the mixture yields the Maxwell–Garnett mixing formula valid for spherical inclusions [29].

However, in the mixing approach applied to estimate ε^m ($m = \mathrm{x}, \mathrm{z}$) of the canopy with height H we used ellipsoidal inclusions to represent the relevant vegetation components "clover leaves" and "grass blades" embedded in the air background host with $\varepsilon_{\mathrm{e}} = 1$. The corresponding semiaxes $a^{\mathrm{C}} \approx b^{\mathrm{C}} \gg c^{\mathrm{C}}$ and $a^{\mathrm{G}} \ll b^{\mathrm{G}} < c^{\mathrm{G}}$ of the oblate clover leaf and grass blade ellipsoid (Fig. 6) are assumed to be $a^{\mathrm{C}} = 1$ cm, $b^{\mathrm{C}} = 0.75$ cm, $c^{\mathrm{C}} = 75$ μm, $a^{\mathrm{G}} = 75$ μm, $b^{\mathrm{G}} = 0.5$ cm, $c^{\mathrm{G}} = H/2$. The fact that the grass blade length exceeds the L-band wavelength $\lambda = 21$ cm does not cause a problem for the application of the dielectric mixing approach because the other grass blade dimensions are still much smaller than λ [30].

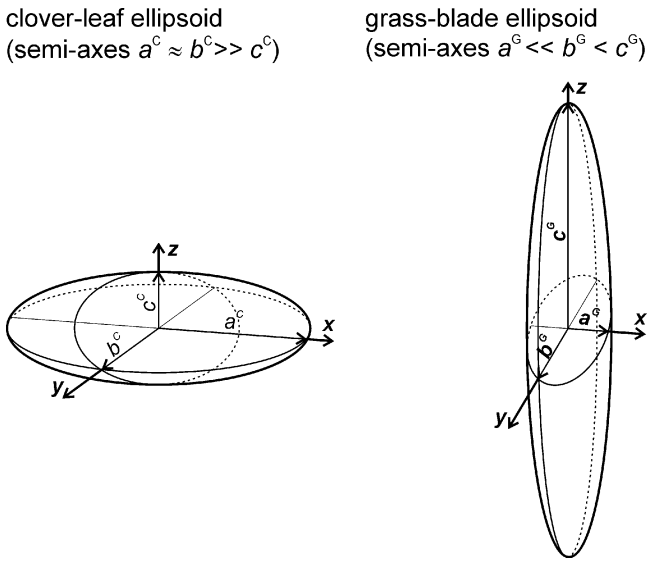

Fig. 6. Ellipsoidal inclusions (clover leaf and grass blade) used in the dielectric mixing model for calculating the effective permittivity of the vegetation. For the evaluation presented in Section IV-C we used $a^{\mathrm{C}} = 1$ cm, $b^{\mathrm{C}} = 0.75$ cm, $c^{\mathrm{C}} = 75$ μm (= leaf thickness), $a^{\mathrm{G}} = 75$ μm (= grass-blade thickness), $b^{\mathrm{G}} = 0.5$ cm, $c^{\mathrm{G}} = H/2$ (H = grass-blade length).

The effective permittivity of a mixture comprising asymmetric inclusions with preferred orientation is represented by a diagonal tensor with eigenvalues (ε^{x}, ε^{y}, ε^{z}), giving permittivities in three dimensions x, y, and z in space. However, given our assumptions concerning the orientation of the vegetation components before and after the hail event, the permittivities for all directions parallel to the soil-surface plane are the same, $\varepsilon^{\mathrm{x}} = \varepsilon^{\mathrm{y}}$. Hence, the effective vegetation permittivity is characterized by the two values ε^m ($m = \mathrm{x}, \mathrm{z}$) determining the propagation of the x and z mode.

The inequality in effective dielectric constants ε^m ($m = \mathrm{x}, \mathrm{z}$) is due to the direction dependent polarizabilities ${\alpha_a}^{\mathrm{C}}$, ${\alpha_b}^{\mathrm{C}}$, ${\alpha_c}^{\mathrm{C}}$ of the clover leaves and grass blades ${\alpha_a}^{\mathrm{G}}$, ${\alpha_b}^{\mathrm{G}}$, ${\alpha_c}^{\mathrm{G}}$ as well as the corresponding depolarization factors ${N_a}^{\mathrm{C}}$, ${N_b}^{\mathrm{C}}$, ${N_c}^{\mathrm{C}}$ and ${N_a}^{\mathrm{G}}$, ${N_b}^{\mathrm{G}}$, ${N_c}^{\mathrm{G}}$, and the assumed orientation of the inclusions. Consequently, expression (13) for the scalar $\varepsilon_{\mathrm{eff}}$ has to be modified to calculate ε^m ($m = \mathrm{x}, \mathrm{z}$).

Two different canopy states are distinguished representing the clover grass during the growth phase and after the hail event on day 190 (Fig. 7). At the end of the growth phase, the canopy is assumed to be composed of randomly oriented clover leaves and upright grass blades (c^{G} along z) with arbitrary orientation around their length-axes c^{G} [Fig. 7(a)]. The damaged canopy after the hail event is described as horizontal grass blades (c^{G} lying in the x-y plane parallel to the soil-surface), randomly oriented with respect to their length-axes c^{G} and their vertical axis a^{G}. Furthermore, the fraction $k^{\mathrm{C}} = 0.3$ of the clover leaves are assumed to be horizontal (c^{C} along z) and randomly oriented around their a^{C} and b^{C} axes. The remaining fraction $(1 - k^{\mathrm{C}}) = 0.7$ of the clover leaves are considered as randomly oriented just like before the hail [Fig. 7(b)]. These simple model

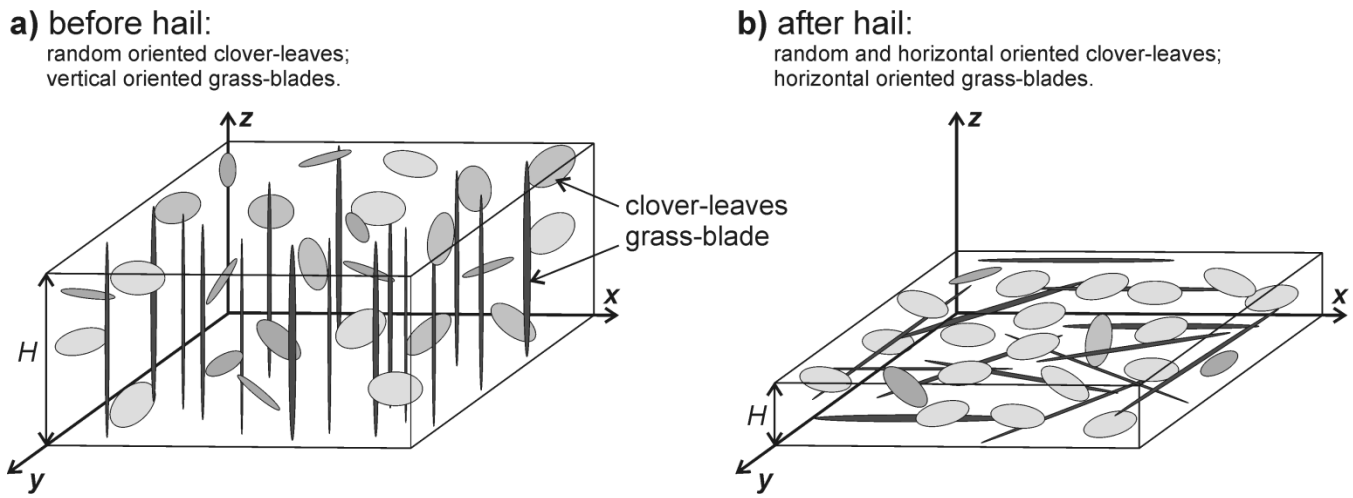

Fig. 7. Sketch of the canopy structure composed of clover leaves and grass blades (a) before and (b) after the hail event.

assumptions are suitable for demonstrating the effect of the hail damage qualitatively (Section IV-C). Nevertheless, the assumed random orientation of the lying grass blades after the hail might be somewhat problematic as local patches of grass with predominant orientations were observed.

Before the hail ε^m ($m = \mathrm{x}, \mathrm{z}$) values are calculated by averaging the clover leaf polarizabilities ${\alpha_a}^{\mathrm{C}}$, ${\alpha_b}^{\mathrm{C}}$, ${\alpha_c}^{\mathrm{C}}$ over the three directions (random leaf orientation). The contribution of the grass blades to ε^{x} is considered by averaging ${\alpha_a}^{\mathrm{G}}$ and ${\alpha_b}^{\mathrm{G}}$ over the horizontal directions and the contribution to ε^{z} is given by ${\alpha_c}^{\mathrm{G}}$ alone. With the number densities n^{C} and n^{G} [m^{-3}] of clover leaves and grass blades, the effective permittivities ε^m ($m = \mathrm{x}, \mathrm{z}$) for the x and the z mode propagating through the canopy are

$$\varepsilon^{\mathrm{x}} = \varepsilon_{\mathrm{e}} + \frac{n^{\mathrm{C}}}{3}\left(\alpha_a^{\mathrm{C}} + \alpha_b^{\mathrm{C}} + \alpha_c^{\mathrm{C}}\right) + \frac{n^{\mathrm{G}}}{2}\left(\alpha_a^{\mathrm{G}} + \alpha_b^{\mathrm{G}}\right) \quad (15)$$

$$\varepsilon^{\mathrm{z}} = \varepsilon_{\mathrm{e}} + \frac{n^{\mathrm{C}}}{3}\left(\alpha_a^{\mathrm{C}} + \alpha_b^{\mathrm{C}} + \alpha_c^{\mathrm{C}}\right) + n^{\mathrm{G}}\alpha_c^{\mathrm{G}}. \quad (16)$$

After the hail [Fig. 7(b)], the fraction k^{C} of the lying clover leaves contributes to ε^{x} with the averaged polarizabilities ${\alpha_a}^{\mathrm{C}}$ and ${\alpha_b}^{\mathrm{C}}$, whereas their contribution to ε^{z} is exclusively determined by ${\alpha_c}^{\mathrm{C}}$. The clover leaf fraction $(1 - k^{\mathrm{C}})$ remaining randomly oriented after the hail contributes the same to ε^{x} and ε^{z} with the averaged polarizabilities over the three directions. The contribution of the lying grass blades to ε^{x} is represented by averaging ${\alpha_b}^{\mathrm{G}}$ and ${\alpha_c}^{\mathrm{G}}$ lying in the x-y plane, and their contribution to ε^{z} is considered by ${\alpha_a}^{\mathrm{G}}$, which is the vertical component. The permittivities ε^m ($m = \mathrm{x}, \mathrm{z}$) of the vegetation layer after the hail are

$$\varepsilon^{\mathrm{x}} = \varepsilon_{\mathrm{e}} + \frac{k^{\mathrm{C}} n^{\mathrm{C}}}{2}\left(\alpha_a^{\mathrm{C}} + \alpha_b^{\mathrm{C}}\right) + \frac{\left(1 - k^{\mathrm{C}}\right) n^{\mathrm{C}}}{3} \cdot \left(\alpha_a^{\mathrm{C}} + \alpha_b^{\mathrm{C}} + \alpha_c^{\mathrm{C}}\right) + \frac{n^{\mathrm{G}}}{2}\left(\alpha_b^{\mathrm{G}} + \alpha_c^{\mathrm{G}}\right) \quad (17)$$

$$\varepsilon^{\mathrm{z}} = \varepsilon_{\mathrm{e}} + \frac{k^{\mathrm{C}} n^{\mathrm{C}}}{1}\alpha_c^{\mathrm{C}} + \frac{\left(1 - k^{\mathrm{C}}\right) n^{\mathrm{C}}}{3} \cdot \left(\alpha_a^{\mathrm{C}} + \alpha_b^{\mathrm{C}} + \alpha_c^{\mathrm{C}}\right) + \frac{n^{\mathrm{G}}}{1}\alpha_a^{\mathrm{G}}. \quad (18)$$

The number densities n^{C} and n^{G} of the clover leaves and grass blades within the canopy are calculated from fresh vegetation mass column density ρ_{veg} [$\mathrm{kg \cdot m^{-2}}$], fractional mass contribution $\nu[-]$ of clover leaves, clover leaf, and grass blade volume $V^{\mathrm{C}} = (4\pi a^{\mathrm{C}} b^{\mathrm{C}} c^{\mathrm{C}})/3$ and $V^{\mathrm{G}} = (4\pi a^{\mathrm{G}} b^{\mathrm{G}} c^{\mathrm{G}})/3$ [m^3], mass density $\rho \approx 950\ \mathrm{kg \cdot m^{-3}}$ of wet vegetation material (without interspaces within the canopy), and canopy height H [m]

$$n^{\mathrm{C}} = \frac{\nu \rho_{\mathrm{veg}}}{V^{\mathrm{C}} \rho H} \quad n^{\mathrm{G}} = \frac{(1 - \nu)\,\rho_{\mathrm{veg}}}{V^{\mathrm{G}} \rho H}. \quad (19)$$

The polarizability component α_a of an ellipsoid with semiaxes a, b, c, volume $V = (4\pi abc)/3$ and permittivity ε_{i} embedded in dielectric background host ε_{e} is [28]

$$\alpha_a = V\left(\varepsilon_{\mathrm{i}} - \varepsilon_{\mathrm{e}}\right) \frac{\varepsilon_{\mathrm{e}}}{\varepsilon_{\mathrm{e}} + N_a\left(\varepsilon_{\mathrm{i}} - \varepsilon_{\mathrm{e}}\right)}. \quad (20)$$

Likewise the b- and c-directed components α_b and α_c of the polarizability $\alpha = (\alpha_a, \alpha_b, \alpha_c)$ can be written, by replacing the depolarization factor N_a with N_b and N_c. Analytical expressions exist for the depolarization factors of ellipsoids

$$N_a = \frac{abc}{2}\int_0^\infty \frac{ds}{(s + a^2)\sqrt{(s + a^2)(s + b^2)(s + c^2)}}. \quad (21)$$

For the depolarization factor N_b (or N_c), interchange b and a (or c and a) in the above integral. For a sphere with radius $r = a = b = c$ this yields $N = N_a = N_b = N_c = 1/3$ [compare (14)].

The permittivity ε_{i} of the inclusions, representing the wet vegetation material, is calculated from a semiempirical formula for the complex dielectric permittivity of leaves [31]

$$\varepsilon_{\mathrm{i}} = 0.522\left(1 - 1.32 m_{\mathrm{d}}\right)\varepsilon_{\mathrm{sw}} + 0.51 + 3.84 m_{\mathrm{d}}. \quad (22)$$

This formula was proven to be applicable in the frequency range from 1–100 GHz for leaves with dry-matter fractions $0.1 \le m_{\mathrm{d}} \le 0.5$ and salinity $\mathrm{S} \approx 10$ ppt (parts per thousand). The saline water permittivity $\varepsilon_{\mathrm{sw}}$ was calculated using a fit for the microwave complex dielectric constant of saline water of temperature T and frequency f using two Debye relaxation wavelengths [32]. In the model calculations, we used $\varepsilon_{\mathrm{sw}} = 34 - \mathrm{j} \cdot 6.8$ as calculated for $S = 7$ ppt, $T = 18.1\ ^{\circ}\mathrm{C}$

(= average temperature during the experiment) and frequency $f = 1.4$ GHz. Temperature variations within the measured range did not affect the model results.

The basic relation $\gamma^m = 2\pi/\lambda \cdot \mathrm{Im}\sqrt{\varepsilon^m}$ is used to calculate the field attenuation coefficients γ^m [m^{-1}] for the two field modes ($m = \mathrm{x}, \mathrm{z}$) from the complex effective permittivities $\varepsilon^m = \varepsilon^{m\prime} - \mathrm{j} \cdot \varepsilon^{m\prime\prime}$. Expressed in terms of $\varepsilon^{m\prime}$ and $\varepsilon^{m\prime\prime}$ this yields

$$\gamma^m = \frac{2\pi}{\lambda}\sqrt{\frac{\varepsilon^{m\prime}}{2}\left(\sqrt{1+\left(\frac{\varepsilon^{m\prime\prime}}{\varepsilon^{m\prime}}\right)^2}-1\right)} \quad (m = \mathrm{x}, \mathrm{z}). \quad (23)$$

The corresponding mode opacities τ^m ($m = \mathrm{x}, \mathrm{z}$) defined to be the negative exponential in Beer's law for the canopy transmissivities of the x and z mode are

$$\tau^m = 2\gamma^m H \quad (m = \mathrm{x}, \mathrm{z}). \quad (24)$$

The relations (15)–(24) allow for estimation of mode opacities τ^m ($m = \mathrm{x}, \mathrm{z}$) of the canopy from the considered structural canopy parameters.

IV. Results and Discussion

A. Measured and Calculated Reflectivities

The reflectivities $r^p{}_{\mathrm{rm}}$ deduced from the radiometer (rm) measurements are calculated from time-series of brightness temperatures $T^p{}_{\mathrm{B}}$ at horizontal and vertical polarization ($p = \mathrm{h}, \mathrm{v}$). The simple relation (2) with $r^p = r^p{}_{\mathrm{rm}}$ and with T_{s} approximated by (3) is used to calculate these data plotted in Fig. 8(a). Fig. 8(b) shows soil reflectivities $r^p{}_{\mathrm{TDR}}$ ($p = \mathrm{h}, \mathrm{v}$) calculated from the permittivity profiles obtained from the *in situ* TDR measurements. The coherent radiative transfer model [24] for stratified dielectrics mentioned in Section III-A was used to calculate $r^p{}_{\mathrm{TDR}}$ from these permittivity profiles.

The soil reflectivities $r^p{}_{\mathrm{TDR}}$ ($p = \mathrm{h}, \mathrm{v}$) calculated from the TDR data are correlated with the reflectivities $r^p{}_{\mathrm{rm}}$ ($p = \mathrm{h}, \mathrm{v}$) based on the L-band brightness temperatures $T^p{}_{\mathrm{B}}$ ($p = \mathrm{h}, \mathrm{v}$) emitted from a smooth bare soil surface. During the vegetation-free period (Fig. 9) $r^{\mathrm{h}}{}_{\mathrm{TDR}}$ and $r^{\mathrm{h}}{}_{\mathrm{rm}}$ for the observation angle $\vartheta_2 = 50°$ are in good agreement. Furthermore, a time delay between the increase of $r^{\mathrm{h}}{}_{\mathrm{TDR}}$ and $r^{\mathrm{h}}{}_{\mathrm{rm}}$ can be observed, which is caused by precipitation at day $\approx$ 149 and 152. The slightly prior increase of $r^{\mathrm{h}}{}_{\mathrm{rm}}$ is a consequence of the higher surface sensitivity of the radiometer measurements compared with the *in situ* TDR measurements. The correlation coefficient between the $r^{\mathrm{h}}{}_{\mathrm{TDR}}$ and $r^{\mathrm{h}}{}_{\mathrm{rm}}$ data is $R = 0.885$. Corresponding correlation coefficients R for the angles $\vartheta_i = 45°, 50°, 55°, 60°$ and both polarizations are listed in Table II. The high correlation between $r^p{}_{\mathrm{TDR}}$ ($p = \mathrm{h}, \mathrm{v}$) and the radiometrically measured reflectivity $r^p{}_{\mathrm{rm}}$ ($p = \mathrm{h}, \mathrm{v}$) during the vegetation-free period justifies the interpretation of $r^p{}_{\mathrm{rm}}$ as reflectivity of the soil. Furthermore, the assumption of a flat soil surface leading to a specular reflectivity is corroborated at least for the vegetation-free period. We assume the soil surface remains electromagnetically flat in the course of the experiment. However, a slightly increasing roughness due to growing vegetation and drying/wettening cycles is expected, but not considered in the presented evaluation.

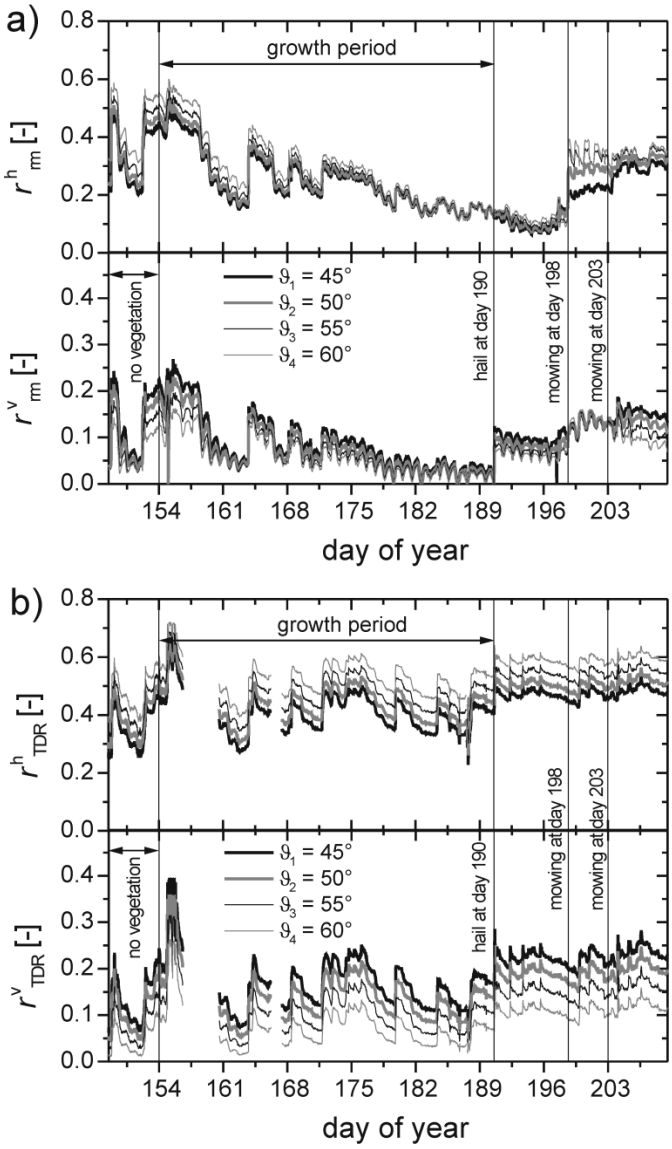

Fig. 8. (a) Time-series of measured reflectivities $r^p{}_{\mathrm{rm}}$ ($p = \mathrm{h}, \mathrm{v}$) of the observed scene. (b) Calculated soil reflectivities $r^p{}_{\mathrm{TDR}}$ ($p = \mathrm{h}, \mathrm{v}$) derived from *in situ* TDR measurements.

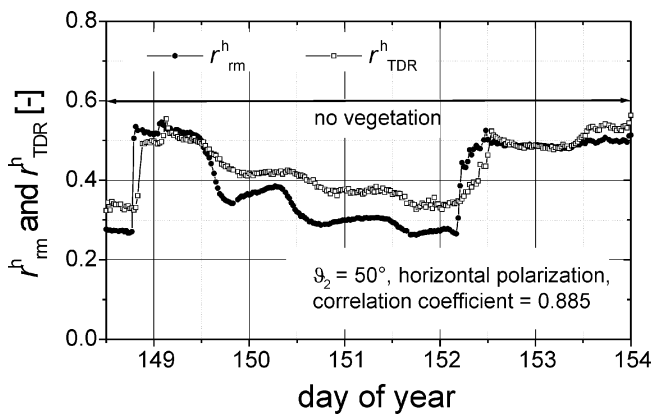

Fig. 9. Soil reflectivities $r^{\mathrm{h}}{}_{\mathrm{TDR}}$ and $r^{\mathrm{h}}{}_{\mathrm{rm}}$ (for h-polarization and $\vartheta_2 = 50°$) calculated from *in situ* TDR data and measured with the radiometer (rm) during the vegetation-free period at the beginning of the experiment (day $\approx$ 149 and 154). Correlation coefficients R of corresponding datasets for h- and v-polarization and ϑ_1 to ϑ_4 are listed in Table II.

TABLE II
CORRELATION COEFFICIENTS R CALCULATED FOR RADIOMETRICALLY MEASURED AND *IN SITU* MEASURED SOIL REFLECTIVITIES $r^{p}{}_{\mathrm{rm}}$ AND $r^{p}{}_{\mathrm{TDR}}$ (p = h, v) DURING THE VEGETATION-FREE PERIOD

ϑ_i [°]	h-polarization	v-polarization
45	0.889	0.882
50	**0.885**	0.875
55	0.881	0.863
60	0.879	0.845

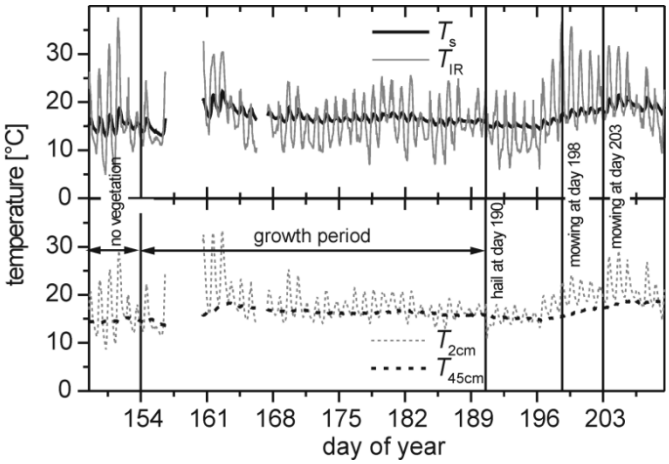

Fig. 10. Time-series of effective soil temperature T_{s}, IR temperature T_{IR} averaged over the four incidence angles ϑ_1 to ϑ_4, and *in situ* soil temperatures $T_{2\ \mathrm{cm}}$ and $T_{45\ \mathrm{cm}}$ measured at 2- and 45-cm depth, respectively.

As can be seen by comparing Fig. 8(a) and (b) the deviation between $r^{p}{}_{\mathrm{TDR}}$ and $r^{p}{}_{\mathrm{rm}}$ (p = h, v) increases with time. The measured reflectivities $r^{p}{}_{\mathrm{rm}}$ (p = h, v) decrease and become less sensitive to the incidence angle ϑ_i whereas the calculated soil reflectivities $r^{p}{}_{\mathrm{TDR}}$ (p = h, v) do not show this trend. This is due to the effect of developing vegetation obscuring the soil. The increasing deviation between the calculated soil reflectivities $r^{p}{}_{\mathrm{TDR}}$ and the measured reflectivities $r^{p}{}_{\mathrm{rm}}$ requires the interpretation of $r^{p}{}_{\mathrm{rm}}$ (p = h, v) as reflectivities of the observed scene (system reflectivity).

The abrupt increase of $r^{\mathrm{h}}{}_{\mathrm{rm}}$ on day 198 when the clover grass was mowed and removed from the field site also supports this assumption. Furthermore, it can be seen that the effect of the hail event on day 190 is highly polarization dependent.

B. Time-Series of Canopy Optical Depth

The measured canopy optical depths $\tau_0^p = \tau^p \cos\vartheta_i$ (p = h, v) at zenith are derived from the presented radiative transfer model [(5) and (6)] as a function of the measured brightness temperature $T^{p}{}_{\mathrm{B}}$ at incidence angle ϑ_i, the temperatures T_{v} and T_{s} of vegetation and soil and the reflectivity $r^{p}{}_{\mathrm{TDR}}$ associated with the soil–vegetation interface.

The soil effective temperature T_{s} (solid black line in Fig. 10) is calculated by approximation (3) using the *in situ* measured temperatures $T_{2\ \mathrm{cm}}$ at 2-cm and $T_{45\ \mathrm{cm}}$ at 45-cm depth (dashed gray and black line). The temperatures T_{IR} (solid gray line), measured with the IR radiometer, were averaged over the four incidence angles ϑ_1 to ϑ_4. The mean spread of T_{IR} ($\max - \min$) measured at these angles was < 0.4 K.

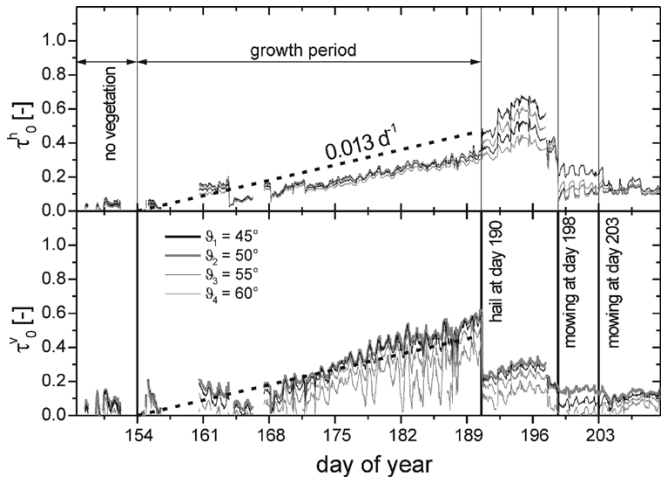

Fig. 11. Time-series of zenith vegetation optical depths $\tau^{p}{}_{0}$ (p = h, v) at incidence angles $\vartheta_1 = 45°$, $\vartheta_2 = 50°$, $\vartheta_3 = 55°$, and $\vartheta_4 = 60°$. Regression for polarization-averaged τ_0 derived from $\tau^{p}{}_{0}$ (p = h, v) at ϑ_2 (black dashed lines).

From the beginning of the experiment to day 154, the temperatures T_{IR} and the *in situ* surface-near temperatures $T_{2\ \mathrm{cm}}$ agree within a couple of degrees. This means that T_{IR} is a measure of soil surface temperature when no vegetation is present. During vegetation development the disagreement between $T_{2\ \mathrm{cm}}$ and T_{IR} increases, showing more distinct daily variations of the IR measurements. If vegetation is present T_{IR} measures the temperature T_{v} of the vegetation, which is determined by the air temperature close to the soil and by evaporation processes at plant surfaces. The *in situ* deep-soil temperature measurements $T_{45\ \mathrm{cm}}$ are least sensitive to meteorological variations.

The calculated soil reflectivities $r^{p}{}_{\mathrm{TDR}}$ [Fig. 8(b)] associated with the air-to-soil transition are used for estimating $\tau^{p}{}_{0}$ (p = h, v). This requires that $r^{p}{}_{\mathrm{TDR}}$ quantifies the reflection at the soil-to-canopy interface as it is understood in the radiative transfer model. This is reasonable due to the low effective permittivity of the vegetation and the observed agreement between $r^{p}{}_{\mathrm{TDR}}$ and the radiometric bare soil reflectivity $r^{p}{}_{\mathrm{rm}}$ before day 154 (Fig. 9 and Table II).

Fig. 11 shows the time-series of the zenith optical depth $\tau^{p}{}_{0}$ (p = h, v) of the vegetation. The values gradually increase during the growth period ($154 < \mathrm{day} < 190$). This behavior will be further discussed in Section IV-C.

First the b-factor of the clover grass, vegetation relating the polarization averaged optical depth τ_0 with the water content ${\rho_{\mathrm{veg}}}^{\mathrm{water}}$ of the vegetation is estimated from our radiometer measurements. The linear relation $\tau_0 = b \cdot {\rho_{\mathrm{veg}}}^{\mathrm{water}}$ is widely used and applicable for a particular vegetation type [33]. The functional dependence of b on the vegetation characteristics was investigated in [16] on the basis of published microwave emission data for various vegetation types and wavelengths between 2.25 and 30 cm. Based on L-band emission data from saturated soil covered with tall grass [34], b was estimated to be between 0.1 and 0.2 $\mathrm{m}^2 \cdot \mathrm{kg}^{-1}$.

To estimate the clover grass b-factor, the polarization averaged optical depth $\tau_0 \equiv (\tau^{\mathrm{h}}{}_{0} + \tau^{\mathrm{v}}{}_{0})/2$ is estimated from the measurements at the angle $\vartheta_2 = 50°$ by calculating the linear

regression $\tau_0(t) = 0.013\,t$ ($[t]$ = days after day 154) approximating the corresponding data τ_0 (black dashed lines in Fig. 11). Combining $\tau_0(t)$ with the linear regression $\rho_{\rm veg}(t) = t \cdot 86\ {\rm g \cdot m^{-2} \cdot d^{-1}}$ derived from the measured fresh vegetation mass column density $\rho_{\rm veg}$ (Fig. 2) and using the vegetation dry-matter fraction $m_{\rm d} = 0.15\ {\rm kg \cdot kg^{-1}}$ allows for eliminating t and relating τ_0 with the specific water mass equivalent ${\rho_{\rm veg}}^{\rm water} = \rho_{\rm veg} \cdot (1 - m_{\rm d})$ stored in the vegetation. From this, we found a reasonable value for the b-factor of the rather dense clover grass vegetation

$$\tau_0 = b \cdot \rho_{\rm veg}^{\rm water} \quad \text{with} \quad b = 0.178\ {\rm m^2 \cdot kg^{-1}}. \tag{25}$$

However, the characterization of the interaction between vegetation and microwave radiation using the single parameter b disregards any effect of vegetation structure on the polarization dependency of the optical depth.

By means of the abrupt change of vegetation structure caused by the hail event on day 190, we found the vegetation optical depths ${\tau^p}_0$ ($p = {\rm h, v}$) changed in a significantly polarization dependent manner. The optical depth ${\tau^{\rm h}}_0$ at h-polarization increased, whereas ${\tau^{\rm v}}_0$ at v-polarization was reduced. This observation is qualitatively explained as the result of the increased permittivity (and loss) seen by an h-polarized wave due to the greater parallel alignment between the predominant orientation of the buckled canopy and the electric field $\boldsymbol{E}^h$ at h-polarization. On the other hand, the decrease of ${\tau^{\rm v}}_0$ is due to reduced permittivity along the direction of the v-polarized field $\boldsymbol{E}^{\rm v}$ as a consequence of more orthogonal alignment between predominant canopy structures and $\boldsymbol{E}^{\rm v}$. These arguments are elaborated more precisely in Section IV-C where the dielectric mixing model presented in Section III-C is evaluated.

The vegetation optical depth ${\tau^{\rm h}}_0$ derived from the measurements at h-polarization after the hail shows a distinct dependency on ϑ_i. This observation cannot be fully explained by the anisotropy of the canopy permittivity. It is suspected that this is a consequence of scattering of the exclusively horizontal field $\boldsymbol{E}^{\rm h} = (E^{\rm hx}, 0)$ at h-polarization (Fig. 5) with lying vegetation structures with dimensions of the order λ [17].

C. Time-Series of Canopy Mode Opacities

Opacities $\tau^m = 2\gamma^m H$ determining the propagation of the x- ($m = {\rm x}$) and the z mode ($m = {\rm z}$) within the canopy are presented in this section. Model calculations are compared with opacities derived from the measurements. The measurement based τ^m ($m = {\rm x, z}$) are governed by the transmissivities Γ^p ($p = {\rm h, v}$) evaluated by the radiative transfer model (5), and the relations (10) and (11). The opacities τ^m ($m = {\rm x, z}$) are plotted in Fig. 12.

At the beginning of the experiment, τ^m values are close to zero as expected for a bare site. The deviations from $\tau^m = 0$ at early vegetation states are mainly due to the inadequacy of the radiative transfer model which does not consider scattering effects [17]. Furthermore, errors in measured temperatures ${T^p}_{\rm B}$ ($p = {\rm h, v}$) and reflectivities ${r^p}_{\rm TDR}$ derived from the *in situ* TDR measurements result in inaccurate τ^m ($m = {\rm x, z}$).

During the growth period both mode opacities τ^m ($m = {\rm x, z}$) increase gradually with time whereas $\tau^{\rm z}$ reaches significantly higher values than $\tau^{\rm x}$. The increase of the opacities is in agreement with the increasing canopy optical depths ${\tau^{\rm v}}_0$ and ${\tau^{\rm h}}_0$ (Fig. 11). Furthermore, the predominantly vertically oriented structure of the developed canopy produces $\tau^{\rm z} > \tau^{\rm x}$. As a consequence of relation (8) the opacity $\tau^{\rm x}$ for the x mode and the optical depth ${\tau^{\rm h}}_0$ measured at h-polarization are identical. As can be seen from comparison of Figs. 12 and 11, the opacity $\tau^{\rm z}$ for the z mode generally exceeds the optical depth ${\tau^{\rm v}}_0$. This is caused by the horizontal field component $E^{\rm vx}$ of the v-polarized field $\boldsymbol{E}^{\rm v} = (E^{\rm vx}, E^{\rm vz})$ (Fig. 5), which is less attenuated by the vertical grass blades.

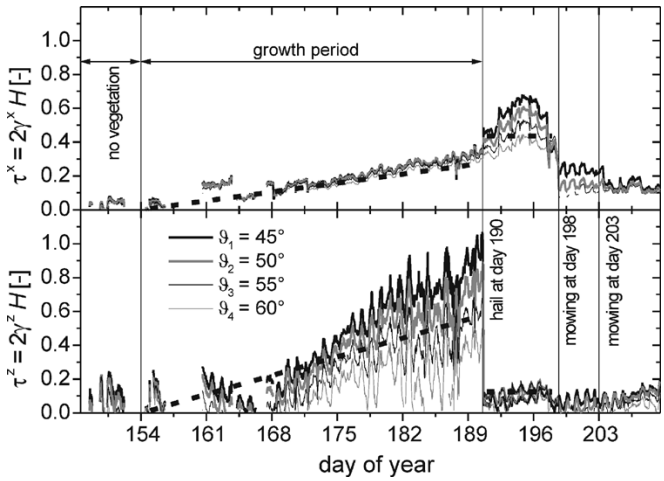

Fig. 12. Opacities $\tau^m = 2\gamma^m H$ relevant for the x mode ($m = {\rm x}$) and the z mode ($m = {\rm z}$) propagating in the canopy. The solid lines show τ^m derived from measurements using the radiative transfer model. The dashed lines are model results calculated with the dielectric mixing model used to characterize the canopy (Section III-C).

Unlike the optical depths ${\tau^p}_0$ ($p = {\rm h, v}$) (Fig. 11), the mode opacities τ^m ($m = {\rm x, z}$) are defined to be properties of the canopy alone. Therefore, τ^m ($m = {\rm x, z}$) should not depend on the incidence angel ϑ_i if the averaged canopy properties do not differ within the corresponding footprints. As can be seen, the ϑ-dependence of $\tau^{\rm x}$ is considerably smaller than the angular dependence of $\tau^{\rm z}$ during the growth period. The situation is *vice versa* for the period between the hail and mowing of the field site ($190 \leq {\rm day} \leq 198$).

This shows that the nonscattering radiative transfer model is adequate when the electric field is at a right angle relative to the main orientation of the vegetation. With increasing alignment between the electric field and the vegetation orientation, scattering becomes important. Furthermore, the $\cos\vartheta_i$-relation between the path length through the vegetation along the line of sight and the perpendicular path length through the vegetation layer [(10) and (11)] leads to an inaccurate description of absorption when the medium is not made up of isotropic scatterers. This might be the reason for the angular dependence of τ^m ($m = {\rm x, z}$) during the growth period and after the hail, respectively.

This observation shows that mode conversion depends on the predominant canopy orientation and incidence angle. Considering such effects would require taking scattering into account in the radiative transfer model [17].

On day 190, τ^{z} is abruptly reduced whereas τ^{x} is increased at least for the data derived from the measurements at the incidence angles ϑ_1 and ϑ_2. This observation is in agreement with the partial conversion of vertical to horizontal oriented vegetation components. The structural change of the canopy due to the hail occurs at the same time as wetting the plants. However, three days after the hail with no precipitation (Fig. 2), the change of the mode opacities can be interpreted as the effect of the structural modification separated from the wetting effect.

Mowing and harvesting on day 198 brought about a rather thin vegetation layer similar to an earlier time during the growth period. Consequently, the opacities τ^m ($m = \mathrm{x}, \mathrm{z}$) are diminished to values observed at the beginning of the vegetation period.

The bold dashed lines in Fig. 12 show calculated opacities τ^m ($m = \mathrm{x}, \mathrm{z}$) utilizing the relations (15)–(24) of the canopy model. The evaluation is performed for the parameters given in Section III-C. The time evolution is considered using the linear fits $H(t) = t \cdot 1.7\ \mathrm{cm\,d^{-1}}$ and $\rho_{\mathrm{veg}}(t) = t\ 86\ \mathrm{g\,d^{-1}}$ to the measured data of the canopy height H and fresh vegetation mass column density ρ_{veg} (Fig. 2).

During the growth period the model represents the experimentally accessed vegetation opacity τ^{x} well. The highest relative deviations occur at early vegetation states and under dry conditions as is the case between day 159 and 163 (Fig. 2). The calculated opacity τ^{z} for the z mode represents the measurements best performed at $\vartheta_2 = 50°$ and $\vartheta_3 = 55°$. The observed increase of τ^{x} as well as the decrease of τ^{z} caused by the structural change of the canopy due to the hail is reproduced by the canopy model.

D. Contribution of Soil Radiation

Growing vegetation reduces the sensitivity of the measured brightness temperature $T^p{}_{\mathrm{B}}$ ($p = \mathrm{h}, \mathrm{v}$) with respect to soil moisture. The fractional contribution Ψ^p of the radiation $T^p{}_3$ emitted from the soil to the total radiation $T^p{}_{\mathrm{B}}$ received by the radiometer can be estimated using the microwave radiative transfer model [Fig. 4 and relation (1)]

$$\Psi^p \equiv \frac{T_3^p}{T_{\mathrm{B}}^p} = \frac{T_3^p}{T_2^p + T_3^p + T_4^p} \quad (p = \mathrm{h}, \mathrm{v}). \tag{26}$$

Fig. 13 shows the contour plot of $\Psi^p(r^p, \tau^p)$ evaluated for the soil reflectivity r^p and the vegetation optical depth τ^p ($p = \mathrm{h}, \mathrm{v}$) characterizing the soil and vegetation state, respectively. Furthermore, a section of the experimental data pairs $[r^p{}_{\mathrm{TDR}}, \tau^p]$ derived from measurements at the incidence angle $\vartheta_2 = 50°$ and h- and v-polarization ($p = \mathrm{h}, \mathrm{v}$) is plotted.

As expected, $\Psi^p(r^p, \tau^p)$ decreases with increasing τ^p. Thereby, the optical depth τ^p of the vegetation can be increased for various reasons such as increasing vegetation column density, structural change of the canopy or measuring at a shallower angle. As expected $\Psi^p(r^p, \tau^p)$ declines when soil reflectivity r^p increases as the consequence of increasing soil water content. This is the result of reduced direct emission $T^p{}_3 \propto 1 - r^p$ from the soil and the higher contribution $T^p{}_4 \propto r^p$ of the radiation emitted downward by the canopy and reflected at the soil surface (Fig. 4).

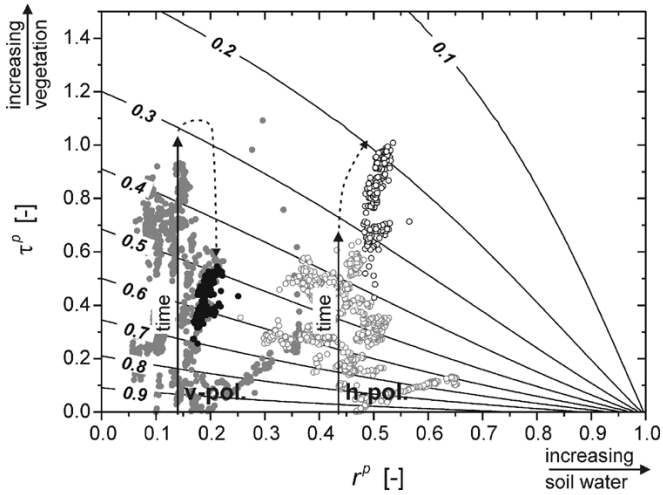

Fig. 13. Shares $\Psi^p(r^p, \tau^p)$ ($p = \mathrm{h}, \mathrm{v}$) of soil radiation to total radiation $T^p{}_{\mathrm{B}}$ plotted in the τ^p-r^p plane together with experimental data $[r^p{}_{\mathrm{TDR}}, \tau^p]$ during the growth period (day 154–190) and after the hail (day 190–198) for $\vartheta_2 = 50°$.

Comparing the data $[r^{\mathrm{h}}{}_{\mathrm{TDR}}, \tau^{\mathrm{h}}]$ (hollow gray circles) and $[r^{\mathrm{v}}{}_{\mathrm{TDR}}, \tau^{\mathrm{v}}]$ (solid gray circles) for h- and v- polarization measured during the growth period ($154 < \mathrm{day} < 190$) with calculated $\Psi^p(r^p, \tau^p)$ shows a decreasing soil moisture sensitivity with time as indicated by the solid arrows. This is in accordance with decreasing soil moisture sensitivity in the course of the vegetation growth period. For both polarizations ($p = \mathrm{h}, \mathrm{v}$), the share Ψ^p of the soil radiation decreases from $\Psi^p \approx 1$ on day 154 to $\Psi^p \approx 0.3$ on day 190. As already mentioned, the hail event increased the vegetation optical depth τ^{h} whereas τ^{v} is diminished. The temporal evolution caused by the hail is indicated by the dashed arrows. As can be seen, the soil moisture sensitivity Ψ^{h} at h-polarization (solid black circles) is decreased and the sensitivity Ψ^{v} at v-polarization (hollow black circles) is enhanced.

V. Conclusion

The evaluation of the simultaneously measured radiometer and *in situ* data revealed polarization-dependent vegetation optical depths τ^p ($p = \mathrm{h}, \mathrm{v}$) correlated with the canopy internal structure. The linear fit to the polarization averaged optical depths τ_0 measured at 50° resulted in a reasonable relationship between the specific water mass equivalent $\rho_{\mathrm{veg}}{}^{\mathrm{water}}$ and τ_0.

Mode opacities τ^m for the x mode ($m = \mathrm{x}$) and the z mode ($m = \mathrm{z}$) propagating through the canopy were derived from measurements and compared with calculations using an anisotropic dielectric mixing model to represent the canopy. The observed change of the mode opacities τ^m ($m = \mathrm{x}, \mathrm{z}$) as the result of structural change within the canopy caused by a hail event was successfully reproduced with this model approach. The results demonstrate that distinct changes in vegetation structure can be measured with L-band radiometry.

However, the experiment showed the likely influence of scattering, which was neglected in our model [17]. The dissimilarity of the vegetation opacities τ^m for the two modes $m = \mathrm{x}$ and z and the correlation of τ^m with the vegetation structure revealed the need to use anisotropic dielectric mixing models to represent the emission properties of vegetation. This brings us to

the conclusion that anisotropic vegetation models are required within soil water retrieval algorithms for use in upcoming satellite missions.

On the other hand, the demonstrated anisotropy of measured opacities τ^m ($m = \mathrm{x}, \mathrm{z}$) offers the possibility for monitoring structural parameters of a vegetation layer. Such information might be useful for future management of extensive agricultural regions. We believe that it is possible to recognize a wide range of vegetation structural changes on agricultural fields and possibly also of forest sites using microwave L-band radiometry.

Furthermore, the results presented contribute toward solving the problem of measuring water content of soils obscured by a vegetation canopy. As shown, through knowledge of the optical depth and the soil reflectivity related to the soil water content, the share of radiation emitted from the soil can be estimated. Thus, the sensitivity of measured L-band radiation with respect to the soil water content can be assessed.

ACKNOWLEDGMENT

The radiometer used in this study was designed and constructed at the Institute of Applied Physics, University of Bern. Success of the demanding field experiment was largely due to J. Leuenberger and H. Wydler from the Institute of Terrestrial Ecology, ETH Zurich. Furthermore, thanks go to T. Green for his editorial work on the manuscript.

REFERENCES

[1] Y. Kerr, P. Waldteufel, J.-P. Wigneron, J.-M. Martinuzzi, J. Font, and M. Berger, "Soil moisture retrieval from space: The Soil Moisture and Ocean Salinity (SMOS) mission," *IEEE Trans. Geosci. Remote Sens.*, vol. 39, no. 8, pp. 1729–1735, Aug. 2001.

[2] T. Schmugge, "Remote sensing of soil moisture," in *Hydrological Forecasting*, M. A. T. Burt, Ed. New York: Wiley, 1985, pp. 101–124.

[3] J.-P. Wigneron, J.-C. Calvet, T. Pellarin, A. A. van de Griend, M. Berger, and P. Ferrazzoli, "Retrieving near- surface soil moisture from microwave radiometric observations: Current status and future plans," *Remote Sens. Environ.*, vol. 85, pp. 489–506, 2003.

[4] D. Entekhabi, E. G. Njoku, P. Houser, M. Spencer, T. Doiron, K. Yunjin, J. Smith, R. Girard, S. Belair, W. Crow, T. J. Jackson, Y. H. Kerr, J. S. Kimball, R. Koster, K. C. McDonald, P. E. O'Neill, T. Pultz, S. W. Running, S. Jiancheng, E. Wood, and J. v. Zyl, "The Hydrosphere State (Hydros) satellite mission: An Earth system pathfinder for global mapping of soil moisture and land freeze/thaw," *IEEE Trans. Geosci. Remote Sens.*, vol. 42, no. 10, pp. 2184–2195, Oct. 2004.

[5] E. A. Sharkov, *Passive Microwave Remote Sensing of the Earth: Physical Foundations*. Berlin, Germany: Springer-Verlag, 2003.

[6] F. Ulaby, R. Moore, and A. Fung, *Microwave Remote Sensing Active and Passive*. Reading, MA: Addison-Wesley, 1981, vol. 1, Microwave Remote Sensing Fundamentals and Radiometry.

[7] ——, *Microwave Remote Sensing Active and Passive*. Reading, MA: Addison-Wesley, 1982, vol. 2, Radar Remote Sensing and Surface Scattering and Emission Theory.

[8] J. R. Wang and T. Schmugge, "An empirical model for the complex dielectric permittivity of soils as a function of water content," *IEEE Trans. Geosci. Remote Sens.*, vol. GE-18, pp. 288–295, 1980.

[9] T. Schmugge, T. Jackson, W. Kustas, and J. Wang, "Passive microwave remote sensing of soil moisture: Results from HAPEX, FIFE, and MONSOON'90," *ISPRS J. Photogramm. Remote Sens.*, vol. 47, pp. 127–143, 1992.

[10] K. Schneeberger, M. Schwank, C. Stamm, P. D. Rosnay, C. Mätzler, and H. Flühler, "Topsoil structure influencing soil water retrieval by microwave radiometry," *Vadose Zone J.*, vol. 3, pp. 1169–1179, 2004.

[11] M. Schwank, M. Stähli, H. Wydler, J. Leuenberger, C. Mätzler, and H. Flühler, "Microwave L-band emission of freezing soil," *IEEE Trans. Geosci. Remote Sens.*, vol. 42, no. 6, pp. 1252–1261, Jun. 2004.

[12] C. Mätzler, "Seasonal evolution of microwave radiation from an oat field," *Remote Sens. Environ.*, vol. 31, pp. 161–173, 1990.

[13] A. A. van de Griend, M. Owe, J. d. Ruiter, and B. T. Gouweleeuw, "Measurement and behavior of dual-polarization vegetation optical depth and single scattering albedo at 1.4- and 5-GHz microwave frequencies," *IEEE Trans. Geosci. Remote Sens.*, vol. 34, no. 4, pp. 957–965, Jul. 1996.

[14] J.-P. Wigneron, M. Parde, P. Waldteufel, A. Chanzy, Y. Kerr, S. Schmidl, and N. Skou, "Characterizing the dependence of vegetation model parameters on crop structure, incidence angle, and polarization at L-band," *IEEE Trans. Geosci. Remote Sens.*, vol. 42, no. 2, pp. 416–425, Feb. 2004.

[15] K. P. Kirdyashev, A. A. Chukhlantsev, and A. M. Shutko, "Microwave radiation of the earth's surface in the presence of a vegetation cover," in *Radio Engineering and Electronic Physics*. Amsterdam, The Netherlands: Scripta, 1979, vol. 24, pp. 37–44.

[16] T. Jackson and T. Schmugge, "Vegetation effects on the microwave emission of soils," *Remote Sens. Environ.*, vol. 36, pp. 203–212, 1991.

[17] B. K. Hornbuckle, A. W. England, R. D. D. Roo, M. A. Fischman, and D. L. Boprie, "Vegetation canopy anisotropy at 1.4 GHz," *IEEE Trans. Geosci. Remote Sens.*, vol. 41, no. 10, pp. 2211–2223, Oct. 2003.

[18] P. Ferrazzoli and L. Guerriero, "Radar sensitivity to tree geometry and woody volume: A model analysis," *IEEE Trans. Geosci. Remote Sens.*, vol. 33, no. 2, pp. 360–371, Mar. 1995.

[19] ——, "Passive microwave remote sensing of forests: A model investigation," *IEEE Trans. Geosci. Remote Sens.*, vol. 34, no. 2, pp. 433–443, Mar. 1996.

[20] C. Mätzler, D. Weber, M. Wüthrich, K. Schneeberger, C. Stamm, and H. Flühler, "ELBARA, the ETH L-band radiometer for soil moisture research," in *Proc. IGARSS*, vol. 5, Toulouse, France, 2003, pp. 3058–3060.

[21] Y. Kerr and E. G. Njoku, "A semiempirical model for interpreting microwave emission from semiarid land surfaces as seen from space," *IEEE Trans. Geosci. Remote Sens.*, vol. 28, no. 3, pp. 384–393, May 1990.

[22] U. Wegmüller, C. Mätzler, and E. G. Njoku, "Canopy opacity models," in *Passive Microwave Remote Sensing of Land-Atmosphere Interactions*, B. J. Choudhury, Ed. Utrecht, The Netherlands: VSP, 1995, pp. 375–387.

[23] J.-Y. Delahaye, P. Golé, and P. Waldteufel, "Calibration error of L-band sky-looking ground-based radiometers," *Radio Sci.*, vol. 37, pp. 11-1–11-11, 2002.

[24] M. Bass, E. W. V. Stryland, R. Williams, and W. L. W, Eds., "Optical properties of films and coatings, Part 11," in *Handbook of Optics*, 2nd ed. New York: McGraw-Hill, 1995, vol. I, pp. 42.9–42.14.

[25] F. Ulaby, R. Moore, and A. Fung, *Microwave Remote Sensing Active and Passive*. Norwood, MA: Artech House, 1986, vol. 3, From Theory to Applications.

[26] B. Choudhury, T. Schmugge, and T. Mo, "A parameterization of effective soil temperature for microwave emission," *J. Geophys. Res.*, vol. 87, pp. 1301–1304, 1982.

[27] J. D. Jackson, *Classical Electrodynamics*, 3rd ed. New York: Wiley, 1999.

[28] A. Sihvola, *Electromagnetic Mixing Formulas and Applications*. London, U.K.: Inst. Elect. Eng., 1999.

[29] A. Sihvola and J. A. Kong, "Effective permittivity of dielectric mixtures," *IEEE Trans. Geosci. Remote Sens.*, vol. 26, no. 4, pp. 420–429, Jul. 1988.

[30] U. Wegmüller, C. Mätzler, and E. Njoku, "Canopy opacity models," presented at the *ESA/NASA Workshop on "Passive Microwave Remote Sensing Research Related to Land-Atmosphere Interactions"*, St. Lary, France, 1993.

[31] C. Mätzler, "Microwave (1–100 GHz) dielectric model of leaves," *IEEE Trans. Geosci. Remote Sens.*, vol. 32, no. 4, pp. 947–949, Jul. 1994.

[32] T. Meissner and F. J. Wentz, "The complex dielectric constant of pure and sea water from microwave satellite observations," *IEEE Trans. Geosci. Remote Sens.*, vol. 42, no. 9, pp. 1836–1849, Sep. 2004.

[33] T. Jackson and P. E. O'Neill, "Attenuation of soil microwave emission by corn and soybeans at 1.4 and 5 GHz," *IEEE Trans. Geosci. Remote Sens.*, vol. 28, no. 5, pp. 978–980, Sep. 1990.

[34] J. R. Wang, J. C. Shiue, T. Schmugge, and E. T. Engman, "The L-band PBMR measurements of surface soil moisture in FIFE," *IEEE Trans. Geosci. Remote Sens.*, vol. 28, no. 5, pp. 906–914, Sep. 1990.

Mike Schwank received the Ph.D. degree in physics from the Swiss Federal Institute of Technology Zürich (ETH), Zürich, Switzerland, in 1999. The topic of his Ph.D. dissertation was "nano-lithography using a high-pressure scanning-tunneling microscope."

From 2000 to 2002, he was a Research and Development Engineer in the field of micro-optics. He is currently a Senior Research Assistant with the Institute of Terrestrial Ecology, ETH-Zürich. His research involves practical and theoretical aspects of radiometry applied to soil moisture detection

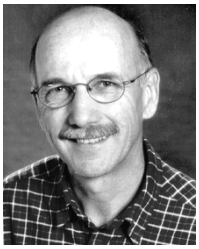

Christian Mätzler (M'96–SM'03) studied physics at the University of Bern, Bern, Switzerland, with subsidiaries in mathematics and geography.

After his doctoral thesis (1974) in solar radio astronomy, he made Postdoctoral Studies at the NASA Goddard Space Flight Center, Greenbelt, MD, and at the Swiss Federal Institute of Technology Zürich, Zürich, Switzerland. He is currently Titular Professor in applied physics and remote sensing, leading the Project Group on Radiometry for Environmental Monitoring, Institute of Applied Physics, University of Bern. His experimental studies have concentrated on surface-based microwave (1–100 GHz) signatures for active and passive microwave remote sensing of snow, ice, soil, vegetation, and atmosphere, including precipitation, clouds, and the boundary layer, and on the development of methods for dielectric measurements of these media, with complementary work at optical wavelengths. He is interested in meteorological applications of remote sensing and in improvements of the physical understanding of the processes involved. Based on the experimental work of his group, he has developed and tested microwave (1–100 GHz) propagation, transmission, emission, scattering, and dielectric models of snowpacks and of the atmosphere.

Dr. Mätzler is a member of the International Glaciological Society.

Massimo Guglielmetti studied environmental sciences at the Swiss Federal Institute of Technology (ETH) Zürich, Zürich, Switzerland. The topic of the master thesis in soil physics (2003) was "quantitative description of tracer distribution in heterogenic sands." He is currently pursuing the Ph.D. degree at ETH.

Since 2004, he has been working as a Ph.D. student at the soil physics group of the Institute of Terrestrial Ecology, ETH. His research field is the investigation of forest soil water content with microwave radiometry.

Hannes Flühler studied at the Department of Forest Sciences, Swiss Federal Institute of Technology (ETH) Zürich, Zürich, Switzerland, and received the Ph.D. degree in 1972. He did his postgraduate studies in soil physics at the ETH Zürich, in 1973, and at the University of California, Riverside, from 1974 to 1976.

From 1977 to 1980, he led the Biophysics Group at the Federal Institute for Forestry Research, and from 1980 to 1983, he chaired the Vegetation and Soil Section at this institute. Since 1983, he has been a Professor of soil physics at ETH Zürich. His research is focused on transport processes in soil, specifically in methodology, but also in relation to environmental applications.